C. R. Chimie 22 (2019) 227–237

Contents lists available at ScienceDirect

Comptes Rendus Chimie

www.sciencedirect.com

Full paper/Mémoire

Improved Cu- and Zn-based catalysts for CO_2 hydrogenation to methanol

Catalyseurs améliorés à base de Cu et Zn pour l'hydrogénation de CO_2 en méthanol

Djaouida Allam [a], Simona Bennici [b, c, *], Lionel Limousy [b, c], Smain Hocine [a]

[a] *Laboratoire de chimie appliquée et de génie chimique, Université Mouloud-Mammeri de Tizi-Ouzou, BP 17 RP, 15000 Tizi-Ouzou, Algeria*
[b] *Université de Haute-Alsace, CNRS, IS2M, UMR 7361, 68100 Mulhouse, France*
[c] *Université de Strasbourg, France*

ARTICLE INFO

Article history:
Received 3 November 2018
Accepted 9 January 2019
Available online 14 February 2019

Keywords:
CO_2 valorization
Polyol synthesis
Methanol synthesis
Oxide catalysts

ABSTRACT

In this study the influence of metal dispersion, spinel formation, and surface properties of binary and ternary catalysts ($CuO–CeO_2$, $ZnO–CeO_2$, $CuO–ZnO–CeO_2$, and $CuO–ZnO–Al_2O_3$) was evaluated. The catalysts prepared by polyol method using polyethylene glycol as a solvent have been tested in the CO_2 hydrogenation to methanol performed at atmospheric pressure. The catalysts prepared by polyol method presented improved properties in terms of metal oxide dispersion, morphology (i.e. sponge-like shape for the CeO_2-containing catalysts), and a large variety of metal and metal oxide species on the surface. Moreover, the $CuO–ZnO–CeO_2$ and $CuO–ZnO–Al_2O_3$ catalysts exhibited a higher activity and selectivity in the methanol synthesis by CO_2 hydrogenation than those displayed by catalysts prepared by more conventional methods.

Mots-clés:
Valorisation du CO_2
Synthèse de polyols
Synthèse du méthanol
Catalyseurs oxydes

RÉSUMÉ

Dans cette étude, des catalyseurs binaires et ternaires ($CuO–CeO_2$, $ZnO–CeO_2$, $CuO–ZnO–CeO_2$ et $CuO–ZnO–Al_2O_3$) ont été utilisés pour l'hydrogénation du CO_2 en méthanol à pression atmosphérique. L'influence de la dispersion des métaux, de la formation de spinelles et des propriétés de surface sur les performances catalytiques a été étudiée. Les catalyseurs, préparés par la méthode polyol en utilisant du polyéthylène glycol en tant que solvant, présentent des propriétés améliorées en termes de dispersion des oxydes métalliques, de morphologie (forme de type éponge pour les catalyseurs contenant CeO_2) et de variétés d'espèces métalliques et d'oxydes métalliques à la surface. De plus, les catalyseurs $CuO–ZnO–CeO_2$ et $Cu–ZnO–Al_2O_3$ présentent une activité et une sélectivité supérieures à celles de catalyseurs préparés par des procédés plus conventionnels pour la synthèse du méthanol par hydrogénation de CO_2.

* Corresponding author. IS2M, CNRS UMR 7361, UHA, 3, rue Alfred-Werner, 68093 Mulhouse cedex, France.
E-mail address: simona.bennici@uha.fr (S. Bennici).

https://doi.org/10.1016/j.crci.2019.01.002

1. Introduction

The concentration of carbon dioxide (a greenhouse gas) inexorably increases in the atmosphere. Various methods are currently examined to decrease the CO_2 concentration or to convert it into valuable chemical products. The use of CO_2 as a feedstock for the synthesis of high added value chemicals is a promising alternative for CO_2 abatement [1,2]. The simplest way to use carbon dioxide is the hydrogenation into valuable compounds, such as methanol (MeOH) and DME (dimethyl ether) [3–8]. Such conversion is often performed on copper-based catalysts. Industrial methanol synthesis is performed by catalytic hydrogenation of syngas ($H_2/CO/CO_2$) over $Cu/ZnO/Al_2O_3$-type catalyst. Unfortunately, the industrial $Cu/ZnO/Al_2O_3$ catalyst is neither active nor selective in CO_2 hydrogenation. Previous published research studies demonstrated that the use of industrial catalysts brings to very low hydrogenation conversions of CO_2 to methanol [9].

This issue can be overcome by developing suitable catalysts, which can effectively convert carbon dioxide to methanol [10–13]. Even if copper-based materials are promising catalysts for the hydrogenation of CO_2 [14–19], further investigations are required for developing new catalytic materials able to give high conversion of CO_2 and improved selectivity to MeOH.

To improve the catalytic performance of methanol synthesis from H_2/CO_2 feeding gas, CuO/ZnO catalysts have been widely modified by adding various activators or other metals (Zr, Si, La, Ti, Cr, Ga, Ce, Fe, Nb, Pd, etc.) [20–25]. The effect of the support was also extensively studied. The type of support affects both CO_2 conversion and methanol selectivity, and, in general, basic oxides such as La_2O_3, Sm_2O_3, Nb_2O_5, In_2O_3, and ThO_2 [26,27] used as supports favor the methanol formation. The preparation methods have also a considerable influence on the catalytic performance [28–30]. Several methods such as coprecipitation [31–35], impregnation [36–38], and sol–gel [38,39] have been developed to prepare copper-based oxide catalysts. Moreover, the coprecipitation synthesis was improved by addition of reducing agents such as chitosane [14] and $NaBH_4$ [15]. Surfactant-assisted coprecipitation [16], solvent-free routine combustion [40], and microfluidic coprecipitation [41] are novel synthesis methods that allow obtaining a good repeatability of the synthesis and an improved homogeneity of the phases present in the catalyst. Other methods, such as impregnation and sol–gel, can also produce catalysts with large specific surface areas and high CuO dispersion [42]. Polyol synthesis represents a good alternative to the classical synthesis methods. In particular, it presents many advantages, such as the possibility to precisely modulate the stoichiometric ratio, the homogeneous mixing of the various components, the low cost, and the short reaction time. Therefore, polyol synthesis reveals to be an attractive technique for the synthesis of nanooxide powders.

$CuO/ZnO/Al_2O_3$-type catalysts obtained by polyol synthesis have been successfully applied in the reverse water gas shift reaction [43], in the alcohol-assisted low temperature methanol synthesis from syngas [44] and in methanol reforming [45].

The polyol method [46,47] permits to synthesize nanosized metallic powders with uniform size distribution and shape [46–48]. In recent years, the polyol method has been studied by many researchers [49–52]. These investigations showed that the crystallite size and shape [46] can be controlled by varying the reduction temperature, the pH, and the nucleation-protective agent concentration [44,49–52]. Until now, and to the best of our knowledge, no attempts to prepare Cu/ZnO catalyst for methanol production using the polyol method have been done. In a typical polyol synthesis, polyols (ethylene glycol, diethylene, glycerol, and tetraethylene glycol) act at the main time as the reaction medium and as the reducing agent. The metal precursor is reduced through a redox reaction between the metal precursors and polyolic species. Therefore, the reaction temperature is an important parameter, because the oxidation potential of polyol chemicals decreases with the increase in the reaction temperature [49,53,54]. Nucleation-protective chemicals such as polyvinylpyrrolidone are occasionally used to prevent sintering and agglomeration of metal particles [53,54]. The various published articles indicate that the choice of the preparation conditions strongly affects the activity of catalysts prepared by the polyol method.

In the present work, the so-called “polyol method” has been used to obtain improved catalytic materials for the hydrogenation reaction of CO_2 to methanol. The influence of metal dispersion, spinel formation, and surface properties of binary and ternary catalysts ($CuO–CeO_2$, $–ZnO–CeO_2$, $CuO–ZnO–CeO_2$, and $CuO–ZnO–Al_2O_3$), prepared by the polyol method using polyethylene glycol as a solvent, is evaluated in the CO_2 hydrogenation to methanol at atmospheric pressure, used as a test reaction.

2. Experimental section

2.1. Preparation of binary and ternary polyol catalysts

Two binary catalysts (labeled $ZnO–CeO_2$ and $CuO–CeO_2$, with Zn/Ce and Cu/Ce molar ratios equal to 1) and two ternary catalysts (labeled $CuO–ZnO–CeO_2$ and $CuO–ZnO–Al_2O_3$, with molar ratios of Cu/Zn/Ce and Cu/Zn/Al equal to 1/1/2) were prepared by the polyol method. The reaction temperature and the choice of the solvent were selected referring to the available investigations reported [44,45]. These experimental conditions seem to favor the formation of nanocrystallites. Different from the synthesis reported in these published studies, nitrate-base

precursors were used in the present research instead of Me acetates. In fact, nitrates do not participate in secondary reactions like those operated by acetates that can react to form methyl acetate and ethyl acetate. First, copper nitrate $Cu(NO_3)_2{\cdot}2.5H_2O$ (Sigma–Aldrich 98%) and/or zinc nitrate $Zn(NO_3)_2{\cdot}6H_2O$ (Sigma–Aldrich 99%) were dissolved in polyethylene glycol $(C_2H_6O_2)_n$ (Sigma–Aldrich 99%, d = 1.13 g/mL). The solution at pH = 2 was then heated up, step by step, and kept under stirring for 1 h at 70 °C, 2 h at 120 °C, and 2 h at 180 °C. Cerium and/or aluminum nitrates ($Ce(NO_3)_3{\cdot}6H_2O$ and/or $Al(NO_3)_2{\cdot}1H_2O$ (Sigma–Aldrich 99%) were then added to the initial solution under vigorous stirring for 4 h at the same temperature (180 °C). The formation of a precipitate was observed. The suspension was cooled down to 100 °C, and NH_4OH was added dropwise to reach a pH of 7. The resulting suspensions were kept under vigorous stirring at 100 °C for 24 h. Finally, the formed gel was dried at 180 °C for 72 h and then calcined in air at 450 °C for 5 h.

2.2. Characterization techniques

Thermogravimetric analyses (TGAs) were performed using a TGA one LF 1100 STARe system from Mettler Toledo. The samples were heated up at 5 °C/min under airflow (100 mL/min) from room temperature to 500 °C.

The X-ray diffraction (XRD) patterns were acquired using a PANalytical MPD X'Pert Pro diffractometer operating with Cu Kα radiation, λ = 0.15406 nm at 40 mA and 45 kV with a scan rate of 2° min^{-1}. Data were collected in the 5–60° 2θ range. The diffraction patterns were analyzed using the Joint Committee on Powder Diffraction Standard. CuO, ZnO, and CeO_2 crystallite sizes were calculated by means of the Scherrer equation:

$$d = \frac{0.89\,\lambda}{\beta\cos\theta} \times \frac{180}{\pi} \quad (1)$$

where d is the diameter of the crystallite, λ the X-ray wave length, and β is the width at half height of the peak.

N_2 adsorption isotherms of the samples were acquired at −196 °C using a Micromeritics ASAP2420 apparatus. Catalyst (0.25 g) was pretreated at 300 °C for 10 h under vacuum (~50 mTorr). The specific surface area was calculated using the multi-Pont BET (Brunauer, Emmett, and Teller) method [55], whereas the pore size distribution was obtained by the BJH (Barrett, Joyner, and Halenda) method [56] to the desorption branch of the isotherm.

Scanning electron microscopy (SEM) coupled with energy dispersive X-ray spectroscopy was performed using a Philips XL 30 instrument (electron acceleration voltage of 15 kV).

X-ray photoelectron spectroscopy (XPS) measurements were performed using a Kratos Axis Ultra DLD spectrometer equipped with a monochromatic microfocused Al Kα (1486.6 eV and Mg Kα=1253.6 eV) X-ray exciting source. The pass energy of the analyzer was set at 40 eV. The adventitious C 1s peak (284.6 eV) was used as internal reference with an accuracy of ±0.3 eV. XPS was used to evaluate the oxidation state of copper, zinc, and cerium species. O 1s, Cu 2p, Zn 2p, Ce 3d, and Al 2p species were quantified by analysis of the survey XPS spectra. The binding energies of C 1s, O 1s, Cu 2p, Zn 2p Ce 3d, and Al 2p were analyzed to identify the associated surface species and the relative atomic concentration.

2.3. Catalytic tests

The catalytic hydrogenation of carbon dioxide to methanol was evaluated in a fixed-bed continuous flow reactor. During each test, 0.3 g of catalyst was pretreated with hydrogen at 300 °C for 3 h. After the reduction step, the catalyst was exposed to a H_2/CO_2 (1/9 volume ratio) flow at different reaction temperatures (190–240 °C). The feeding mixture and the reaction products were analyzed online with a gas chromatograph (Shimadzu GC-2014) equipped with flame ionization detector (FID) and thermal conductivity detector (TCD). CO_2 conversion (X) and products' selectivity were calculated as follows, using the quantitative correction factor (k_f) and peak area (S) for the different species:

$$X\,CO_2(\%) = \frac{S_{CO_2\ in} - S_{CO_2\ out}}{S_{CO_2\ in}} \times 100 \times k_{f_{CO_2}} \quad (2)$$

$$CH_3OH\ selectivity\ (\%) = \frac{S_{CH_3OH\ out}}{X\,CO_2} \times 100 \times k_{f_{CH_3OH}} \quad (3)$$

$$CH_4\ selectivity\ (\%) = \frac{S_{CH_4\ out}}{X\,CO_2} \times 100 \times k_{f_{CH_4}} \quad (4)$$

3. Results and discussions

3.1. Characterization of catalysts

3.1.1. Thermal behavior

The thermal behavior of catalysts before and after calcinations is shown in Fig. 1. The sample mass continuously decreased with the temperature. For the catalysts before calcination, the TGA curves showed three main events connected to the decomposition of residual precursors (Fig. 1a) (indeed, the most part of the precursors has been eliminated by the thermal treatment during the synthesis).

A first mass variation in the 0.5–2.5% range was observed up to 250 °C and was attributed to the loss of water (physisorbed and chemisorbed) as well as to the decomposition of residual nitrates from the precursors. The second and highest mass loss (0.5–3%) between 250 and 350 °C was probably related to the elimination of polyethylene glycol. The third step, at temperature greater than 350 °C, corresponded to the lowest mass loss (0.5%) and was attributed to the decomposition of hydroxyl groups, leading to metal oxide formation. After calcinations (Fig. 1b), the catalyst showed a low mass loss (<2%), attributed to the release of physisorbed water (<150 °C), and the decomposition of carbonates formed by a reaction

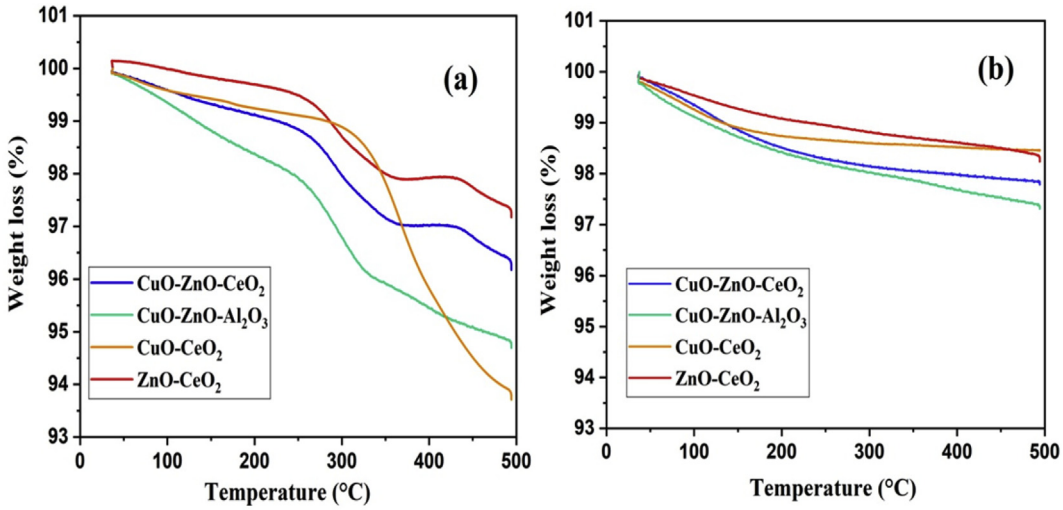

Fig. 1. TGA profiles of the catalyst (a) before calcination and (b) after calcination at 500 °C.

with atmospheric CO_2. The presence of carbonates was observed also by XPS (as described in Section 3.1.3).

3.1.2. Structure and morphology of the catalysts

The X-ray diffractograms of the calcined bimetallic and trimetallic catalysts are displayed in Fig. 2. For the three calcined catalysts, CuO–CeO_2, ZnO–CeO_2, and CuO–ZnO–CeO_2, only the diffraction peaks relative to the CuO, ZnO, and CeO_2 phases could be clearly identified. The diffraction peaks centered at 28.6°, 33.1°, 47.5°, 56.3°, 59.1°, and 69.0° 2θ, corresponding respectively to the (111), (200), (220), (311), (222), and (400) diffraction planes of cubic CeO_2 [57,58], were observed for the ZnO–CeO_2, CuO–CeO_2, and CuO–ZnO–CeO_2 catalysts. For the ZnO–CeO_2 and CuO–ZnO–CeO_2 samples, diffractions at 31.7°, 34.5°, 36.2°, 62.9°, and 69.0° 2θ indicated the presence of hexagonal ZnO [31,57,59,60] and corresponded respectively to the (100), (002), (101), (103), and (201) planes. The cubic CuO phase [31,57,59], present in the CuO–CeO_2 and CuO–ZnO–CeO_2 samples, was characterized by broad diffraction lines at 35.5° and 38.7° 2θ corresponding to the (−111) and (111) planes. Broad diffraction lines at 2θ = 35.5°, 38.7°, 61.5°, and 68.1° indicated the presence of CuO and correspond respectively to the (−111), (111), (−202), (−113), and (−220) planes. In addition to CuO, $CuAl_2O_4$ and $ZnAl_2O_4$ spinels could be identified in the CuO–ZnO–Al_2O_3 sample. The diffraction peaks of $CuAl_2O_4$ and $ZnAl_2O_4$ were superposed and placed at 31.2°, 36.8°, 55.6°, 59.3°, and 65.2° 2θ. No diffraction peaks relative to ZnO could be identified in CuO–ZnO–Al_2O_3; all zinc was present as spinel $CuZnAl_2O_4$.

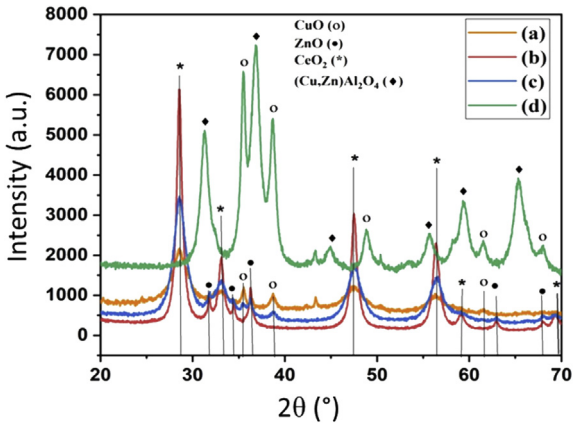

Fig. 2. XRD patterns of calcined catalysts: (a) CuO–CeO_2, (b) ZnO–CeO_2, (c) CuO–ZnO–CeO_2, and (d) CuO–ZnO–Al_2O_3.

The metal oxide crystallite dimensions were evaluated applying the Scherrer equation to the main diffraction peak of each phase, and the results are reported in Table 1. ZnO crystallite size of 20–30 nm was calculated in the binary ZnO–CeO_2 catalyst. CuO crystallites, in the 10–20 nm dimension range, were detected for the CuO–CeO_2 catalyst (Table 2). The CuO (6 nm) and ZnO (12 nm) crystallites were much smaller for the ternary CuO–ZnO–CeO_2 sample, indicating that the presence of zinc and copper oxides together ameliorates the oxide distribution and dispersion during the synthesis procedure.

The nitrogen adsorption–desorption isotherms of the various polyol samples (acquired at −196 °C) are shown in Fig. 3a. The catalysts isotherm shows a continuous increase in adsorbed nitrogen over the whole P/P_0 range, with a relatively steep increase at $P/P_0 \geq 0.85$. For all catalysts, the N_2 adsorption isotherms (Fig. 3b) were of type II [61] with no plateau at high P/P_0 values, which is usually observed for materials with macropores or interparticular mesoporosity [62]. H4-type hysteresis was observed for the CuO–ZnO–Al_2O_3 sample, and H3-type for the ZnO–CeO_2, CuO–CeO_2, and CuO–ZnO–CeO_2 samples [63]. These types of hysteresis are typical of lamellar compounds or slit-shaped pores [64].

All materials presented relatively low porous volumes (Table 1, third column), as expected for this kind of preparation that produces bulk oxides. Fig. 3b represents the

Table 1
Morphological and structural properties of the catalysts.

Sample	S_{BET} ($m^2\ g^{-1}$)	V_{pore} ($cm^3\ g^{-1}$)	D_{pore}[a] (nm)	Crystallite size with XRD analysis[b] (nm)			
				CuO	ZnO	CeO_2	$Cu,ZnAl_2O_4$
$CuO–CeO_2$	32	0.07	17	10–20	–	5	–
$ZnO–CeO_2$	18	0.03	20	–	20–30	5	–
$CuO–ZnO–CeO_2$	38	0.12	22	6	12	5	NA
$CuO–ZnO–Al_2O_3$	30	0.04	23	20–30	–	–	30–40

[a] Determined from desorption branch of N_2 adsorption isotherm by the BJH model.
[b] Crystallite size calculated by the Scherrer equation.

Table 2
Surface elements' presence as determined by XPS analysis.

Orbital	$CuO–ZnO–CeO_2$			$CuO–ZnO–Al_2O_3$		
	Binding energy (eV)	Species	At (%)	Binding energy (eV)	Species	At (%)
C 1s	284.98	C–C	16.54	285.01	C–C	2.46
	286.53	C–OR	0.60	286.56	C–OR	0.28
	287.98	C=O	2.55	288.01	C=O	0.40
	289.48	O=C–O	4.62	289.47	O=C–O	0.89
O 1s	529.49	Cu–O	6.97	529.80	Cu–O	9.02
	529.43	Ce^{4+}/Cu–O	29.07	531.71	Al–O	33.22
	530.90	Ce^{3+}/Zn–O	4.17	530.80	Zn–O	8.51
	531.90	$(CO_3)^{2-}$	7.04	531.40	$(CO_3)^{2-}$	2.64
Cu 2p	932.75	Cu^{2+}/Cu^{+}	5.87	933.61	Cu^{2+}	4.31
	934.91	Cu^{2+}/Cu^{+}	0.97	935.66	Cu^{2+}	1.42
	940.92	Cu^{2+}/Cu^{+}	0.99	940.87	Cu^{2+}	1.68
	943.54	Cu^{2+}/Cu^{+}	0.78	943.43	Cu^{2+}	1.65
Zn 2p	1021.56	ZnO	0.53	1021.87	ZnO	7.71
Ce 3d	881.00 (V^0)	Ce^{3+}	0.92	–	–	–
	899.39 (U^0)					
	882.44 (V)	Ce^{4+}	4.42	–	–	–
	900.76 (U)					
	884.95 (V^I)	Ce^{3+}	3.80	–	–	–
	903.20 (U^I)					
	888.70 (V^{II})	Ce^{4+}	5.33	–	–	–
	907.36 (U^{II})					
	898.16 (V^{III})	Ce^{4+}	4.82	–	–	–
	916.34 (U^{III})					
Al 2p	–	–	–	74.47	Al^{3+}	24.86

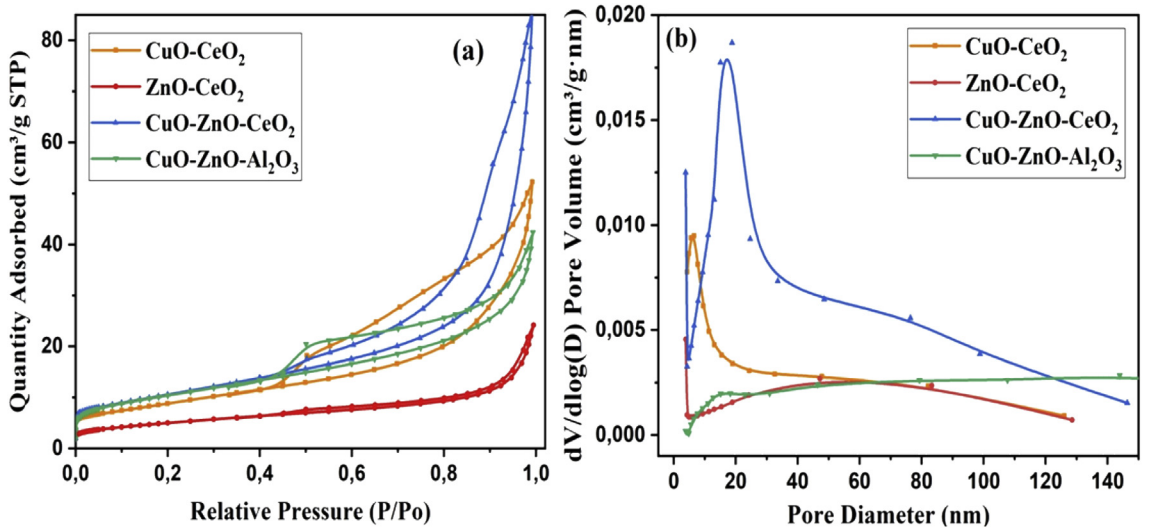

Fig. 3. (a) N_2 adsorption–desorption isotherms and (b) pore size distribution of all samples.

pore size distribution of the catalysts. All catalysts presented a certain mesoporosity centered in the 17–23 nm range. The presence of macropores (up to 150 nm) was observed for the three samples containing CeO_2, whereas even larger pores were present in the CuO–ZnO–Al_2O_3 sample.

The presence of copper oxide seems to improve the specific surface area of the catalysts (in the 30–38 $m^2\ g^{-1}$ range), as reported in Table 1. The catalyst with the lower surface area (18 $m^2\ g^{-1}$) was ZnO–CeO_2. This behavior is probably connected to the improved pore volume that can be obtained in the presence of the copper precursor, which end up into a higher internal surface area. Indeed, ZnO–CeO_2 presented the lowest pore volume and the hysteresis between the adsorption and desorption isotherms was almost absent.

The morphology of the different calcined CuO–CeO_2, ZnO–CeO_2, CuO–ZnO–CeO_2, CuO–ZnO–Al_2O_3 samples was investigated by SEM, and the acquired images are presented in Fig. 4. The catalysts containing CeO_2 showed a sponge-like morphology, as reported in Fig. 4 for the CuO–CeO_2 (a–c), ZnO–CeO_2 (d–f), and CuO–ZnO–CeO_2

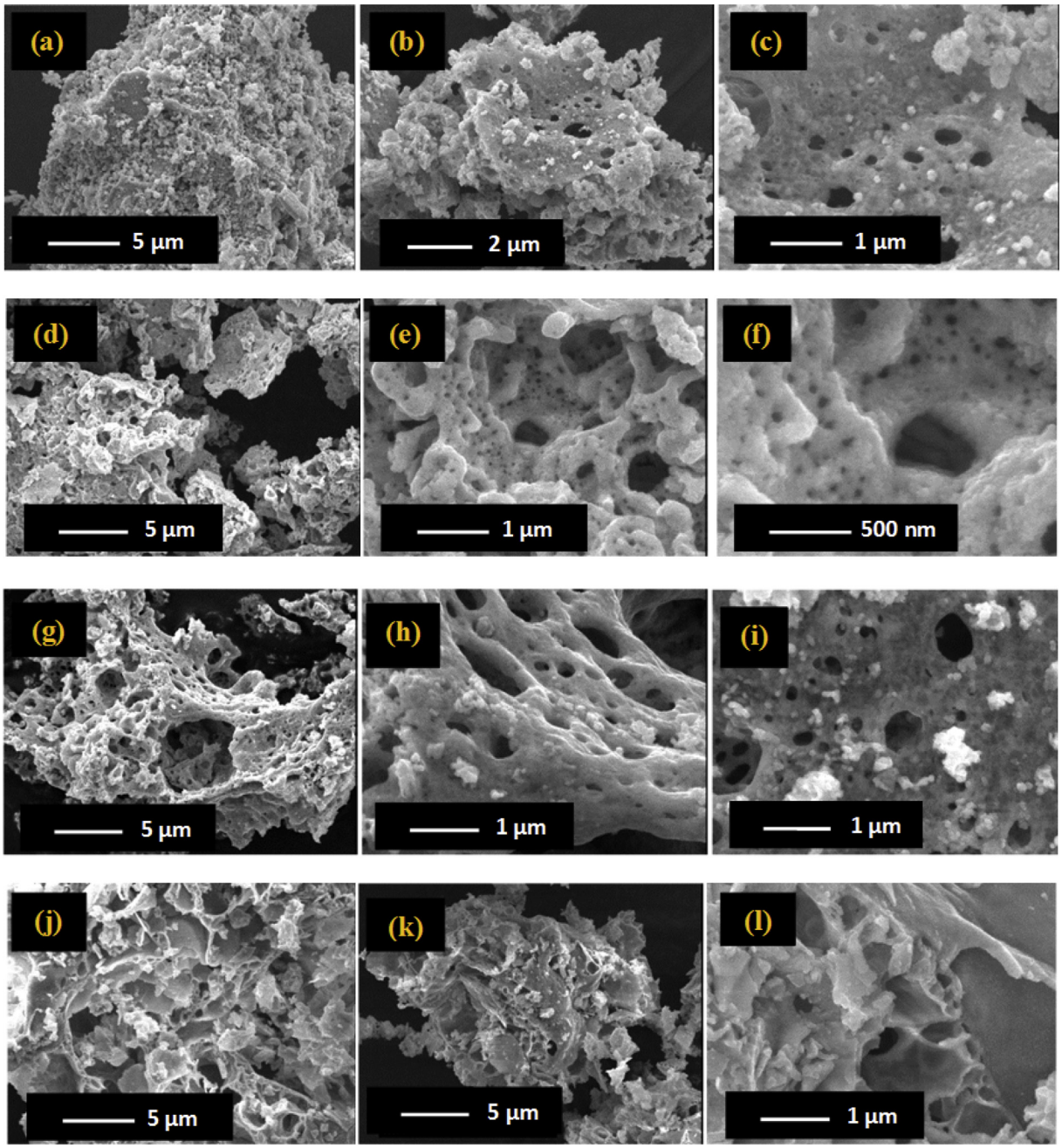

Fig. 4. SEM images at different magnification of all catalysts (a–c) CuO–CeO_2, (d–f) ZnO–CeO_2, (g–i) CuO–ZnO–CeO_2, and (j–l) CuO–ZnO–Al_2O_3.

(g–i) samples. The three ceria-containing samples were characterized by the presence of round-shaped cavities and pores of various dimensions, well distributed in the sample catalyst structure. CuO–ZnO–Al_2O_3 presented a different morphology (Fig. 4j–l), with well-developed and thin plate-shaped bonded sheets in the 1–5 μm dimension interval. The presence of macropores was confirmed by these images and linked to the formation of gas bubbles during the preparation step, because of the decomposition of the metal oxide precursors.

Energy dispersive X-ray spectroscopy analysis showed a very homogeneous distribution of the different oxides in all samples.

3.1.3. Chemical composition and surface properties

Photoelectron spectroscopy was used to evaluate the oxidation state of copper, zinc, and cerium species in the CuO–ZnO–CeO_2 and CuO–ZnO–Al_2O_3 calcined catalysts, as well as to evaluate their surface chemical composition (Table 2). All elements (Cu, Zn, Ce, Al, and O) were present at the sample surface (Table 2). The survey XPS acquisition permitted to quantify the various atoms (O 1s, Cu 2p, Zn 2p, Ce 3d, and Al 2p) for the two trimetallic catalysts. Clear differences in the surface elements were observed for the two samples. Zn concentration was particularly low on the surface of the CuO–ZnO–CeO_2 sample (0.53%). On the contrary, a large amount of carbon was detected on its surface (24.31%). Because the most part of carbon on the surface of CuO–ZnO–CeO_2 could be assigned to residual contamination or hydrocarbon chains, as described later in this section, these results can suggest that the carbon pollution presented a higher affinity for Zn, thus selectively covered at the extreme surface. Less dramatic differences were identified in the CuO–ZnO–Al_2O_3 sample that showed similar concentrations of copper and zinc on the surface.

No N 1s XPS peak (generally placed around 400.3 eV) related to nitrate (NO_3^-) species (salt precursors) has been identified for the CuO–ZnO–Al_2O_3 and CuO–ZnO–CeO_2 catalysts, as an indication of the complete decomposition of nitrated after calcination.

The binding energies of C 1s, O 1s, Cu 2p, Zn 2p Ce 3d, and Al 2p of the two trimetallic catalysts are listed in Table 2, as well as the associated surface species and their atomic concentration.

The Cu 2p spectrum of both CuO–ZnO–CeO_2 and CuO–ZnO–Al_2O_3 (Fig. 5) catalysts presented the characteristic spin–orbit split Cu $2p_{1/2}$ and Cu $2p_{3/2}$ peaks, with their shake-up satellites of Cu^{2+} [65]. Binding energies, in the 932.0–932.8 and 933.2–934.6 eV ranges, are characteristics of Cu^+ and Cu^{2+}, respectively [66,67]. These two contributions could be identified in the CuO–ZnO–CeO_2 sample (upper spectrum in Fig. 5). The large and strong peak centered at 932.7 eV was then attributed to Cu^{2+} and/or Cu^+ species, whereas the small and broad peak centered at 934.9 eV was assigned to Cu^{2+} species [68]. For the CuO–ZnO–Al_2O_3 sample (Fig. 5), the Cu $2p_{3/2}$ peak presented two contributions characteristic of Cu^{2+} species; the first one was observed at 933.61 eV and related to copper oxide, whereas a second contribution, at a higher binding energy (935.66 eV), was assigned to Cu^{2+} in the $CuAl_2O_4$-like environment (the presence of the spinel structure, $CuAl_2O_4$, was also observed by XRD analysis). Indeed, the shift to higher binding energy is indicative of a charge transfer from Cu^{2+} toward $Al_2O_4^{2-}$ [69,70]. The intensity ratio of the satellite peak to the related main peak (I_{sat}/I_{pp}) was 0.17, for the CuO–ZnO–CeO_2 catalyst and 0.44 for CuO–ZnO–Al_2O_3. The lower I_{sat}/I_{pp} value is characteristic of well-dispersed copper oxide species in an octahedral coordination environment, whereas the higher value is symptomatic of a coordination change, most probably because of the formation of the spinel [71]. In addition, the contribution at around 529 eV of the O 1s spectra can also be assigned to the presence of Cu^{2+} and Cu^+ (see Table 2).

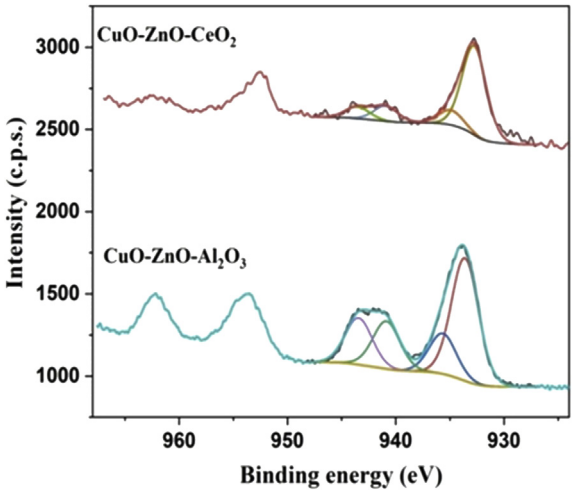

Fig. 5. Cu 2p XPS spectra of CuO–ZnO–CeO_2 and CuO–ZnO–Al_2O_3 samples.

The Zn $2p_{3/2}$ XPS spectra for the two trimetallic catalysts were characterized by one defined peak around 1021–1022 eV that could be assigned to Zn^{2+} species. The presence of ZnO has also been confirmed by the O 1s band centered at 530.8 eV [72,73]. The XPS signal of CuO–ZnO–CeO_2 was much less intense than that of CuO–ZnO–Al_2O_3, indicating the higher ZnO concentration on the CuO–ZnO–Al_2O_3 surface (8.68%$_{atom}$ for CuO–ZnO–Al_2O_3 and 0.53%$_{atom}$ for CuO–ZnO–CeO_2 catalysts.

The presence of carbon was detected on the surface of both samples. The C 1s spectra are reported in Fig. 6 for the CuO–ZnO–CeO_2 and CuO–ZnO–Al_2O_3 catalysts. In both cases the spectra were composed of two contributions: the first, centered at 289.5 eV was assigned to carbonate species, whereas the more intense band, at around 285 eV, to residual contamination or hydrocarbon chains, probably deriving from the polyethylene glycol used during the catalyst synthesis. Indeed, cerium oxide and reduced cerium are known to react with CO_2 (e.g., present in the atmosphere) and give rise to carbonate species on the surface [74]. The carbonate band was much less intense for the CuO–ZnO–Al_2O_3 catalyst, and the corresponding atomic percentage was about 1.3% instead of 7.2% for the CuO–ZnO–CeO_2 catalyst. The presence of carbonates was also confirmed by the O 1s XPS band centered at high binding energies (531.9 and 531.4 eV, respectively for CuO–ZnO–CeO_2 (Fig. 7a) and CuO–ZnO–Al_2O_3 (Fig. 7b)).

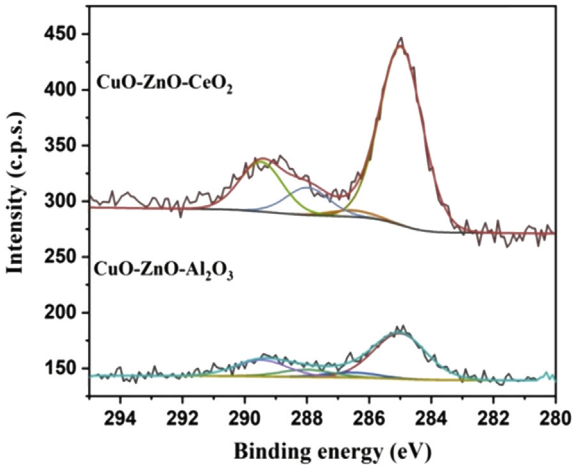

Fig. 6. C 1s XPS spectra of CuO–ZnO–CeO_2 and CuO–ZnO–Al_2O_3 samples.

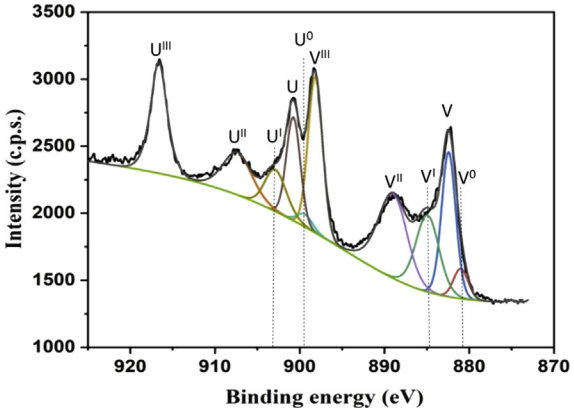

Fig. 8. Ce 3d XPS spectra of the CuO–ZnO–CeO_2 sample.

The XPS spectrum of Ce 3d for the CuO–ZnO–CeO_2 sample is depicted in Fig. 8 and presents a complex behavior. The split of the band into numerous peaks is because of the hybridization between the final state Ce 4f orbitals and the O 2p oxygen orbital [75]. In Fig. 8, the peaks are identified by V and U labels, indicating respectively the spin–orbit coupling three $d^{3/2}$ and $3d^{5/2}$ [76], by applying the convention introduced by Burroughs et al. [77] in 1976. Ce 3d spectrum can be decomposed in five doublets, (U^{III}, V^{III}), (U^{II}, V^{II}), (U^{I}, V^{I}), (U°, V°), and (U, V), corresponding to the emissions from the spin–orbit split $3d^{3/2}$ and $3d^{5/2}$ core levels [76–78]. The five doublets were assigned to different final states of tetravalent (Ce^{4+}) or trivalent (Ce^{3+}) in Ce compounds (see Table 3); U^{III} (916.6 eV) and V^{III} (898.2 eV) were because of a Ce $3d^9 4f^0$ O $2p^6$ final state, U^{II} (907.4 eV) and V^{II} (888.8 eV) to a Ce $3d^9 4f^1$ O $2p^5$ final state, U^{I} (903.2 eV) and V^{I} (884.9 eV) to a Ce $3d^9 4f^1$ O$2p^6$ final state, U° (899.3 eV) and V° (881.0 eV) to a Ce $3d^9 4f^2$ O $2p^5$ final state, and U (900.8 eV) and V (882.4 eV) to a Ce $3d^9 4f^2$ O $2p^4$ final state. Specifically the well-defined U^{III} peak at 916.6 eV was characteristic of the presence of Ce^{4+} [76].

3.2. Catalytic tests

To verify the catalytic performances of the binary and ternary polyol catalysts in relation to the chemical composition, oxide structure, and surface properties, CO_2 hydrogenation to methanol was used as a test reaction. The tests were carried-out at atmospheric pressure by feeding the tubular reactor with a H_2/CO_2 =1/9 mixture. Methanol and methane were the main carbon containing products, whereas only traces of carbon monoxide were detected.

The activity of the four catalysts was compared at 240 °C (Fig. 9). The binary catalysts, CuO–CeO_2 and ZnO–CeO_2, did not show any catalytic activity (CO_2 conversion <2%). The ternary CuO–ZnO–CeO_2 and Cu–ZnO–Al_2O_3 catalysts showed similar conversion curves as a function of time, with stabilization of their activity after 4 h of reaction. The CuO–ZnO–CeO_2 catalyst showed the best result with a maximum conversion of about 20%, whereas Cu–ZnO–Al_2O_3 reached a conversion not exceeding 14%. The enhanced activity of the ternary catalysts is attributed to the synergistic effect between CuO and ZnO, as already known from the literature [79–81]. The higher activity of the CuO–ZnO–CeO_2 catalyst can be attributed to both the

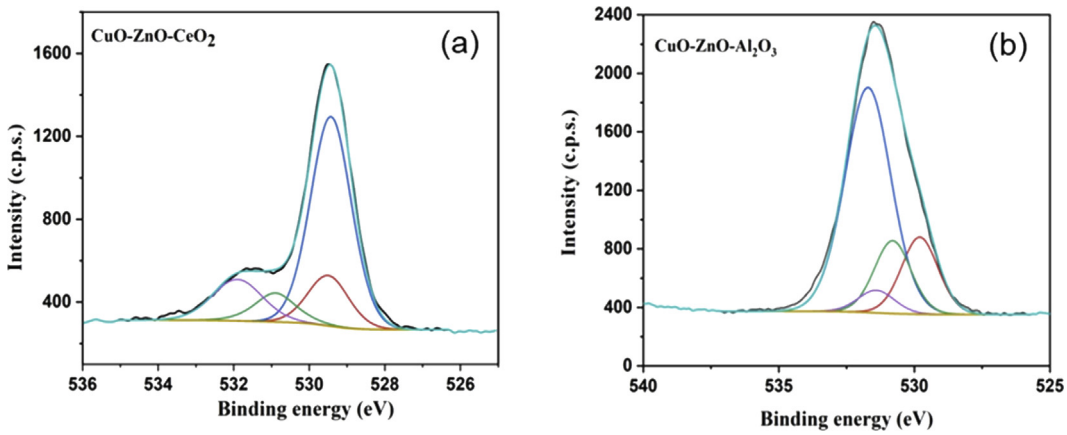

Fig. 7. O 1s XPS spectra of (a) CuO–ZnO–CeO_2 and (b) CuO–ZnO–Al_2O_3 samples.

Table 3
Catalytic performances in the hydrogenation of CO_2, obtained on the catalysts prepared.

Type of catalyst	Preparation method	T (°C)	P (MPa)	R (H_2/CO_2)	CO_2 conversion (%)	CH_3OH Selectivity (%)	Reference
$CuO-ZnO-Al_2O_3$	Polyol method	240	0.1	9.0	14	86	This work
$CuO-ZnO-CeO_2$	Polyol method	240	0.1	9.0	20	90	
$CuO/ZnO/Al_2O_3$	Solvent-free routine	240	3.0	3.0	16	64	[40]
$CuO/ZnO/ZrO_2$	Surfactant coprecipitation method	240	3.0	3.0	12	33	[16]
$CuO-ZnO-ZrO_2$ (M)	Coprecipitation microfluidic	240	5.0	3.0	9	47	[41]
$CuO-ZnO-ZrO_2$ (pH)	Coprecipitation at controlled pH				14	50	
CZZ0	Precipitation/reduction method	230	5.0	3.0	17	67	[15]
CZZ3	($NaBH_4$)				15	62	
CZZ5					15	67	
Cu/ZnO	Coprecipitation	240	3.0	3.0	17	78	[83]
$10Cu^-/CeO_2$	Coprecipitation + impregnation	230	3.0	3.0	4	66	[84]
$0.5Pd-10Cu/CeO_2$					6	49	
$2Pd-10Cu/CeO_2$					15	29	
$CuO-ZnO-TiO_2-ZrO_2$	Coprecipitation (oxalate)	240	3.0	3.0	17	44	[60]
Cu/ZnO	Impregnation	240	0.1	9.0	5	12	[42]
$Cu-Zn/SiO_2$	Impregnation	250	2.0	3.0	2	66	[1]
5%CuZn/rGo	Incipient wetness impregnation	250	1.5	3.0	14	3	[19]
10%CuZn/rGo					26	5	
20%CuZn/rGo					19	9	
$CuO/ZnO/Al_2O_3$ (Cp)	With internal cooling water	240	3.0	3.0	52	69	[85]
$CuO/ZnO/Al_2O_3$ (Cp)	Without internal cooling water						
$Cu/ZrO_2 + CaO$	Wetness impregnation	250	0.1	3.0	3	1	[86]

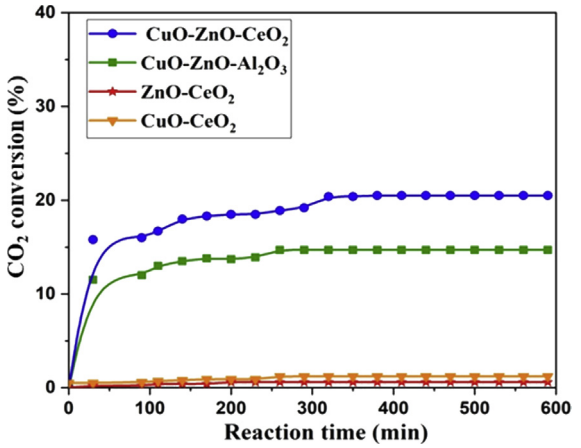

Fig. 9. CO_2 conversion as a function of the time of reaction. Reaction conditions: $CO_2/H_2 = 1/9$, $T = 240$ °C, flow = 1 L h^{-1} and $P = 1$ atm.

basicity of CeO_2 [82], which favors the adsorption of CO_2 (i.e. an acid molecule), and the enhanced reducibility of the system, leading to the increase in the number of active sites after reducing pretreatment operated in situ before the reaction tests. Moreover, in the $Cu-ZnO-Al_2O_3$ catalyst, copper and zinc oxides were not fully available because of the formation of the $CuAl_2O_4$ and $ZnAl_2O_4$ spinels, as shown by XRD. Indeed, zinc and copper trapped into the spinel cannot enter in intimate contact and their synergistic catalytic effect [80–82] cannot be deployed.

On the most active catalyst ($CuO-ZnO-CeO_2$), further tests at different reaction temperatures were performed. The CO_2 conversion as a function of time is plotted in Fig. 10a for the tests performed in the 190–240 °C temperature range. At the beginning the curves presented an activation step, characterized by a steep section of the conversion curve; after 1 h of reaction, the change in slope

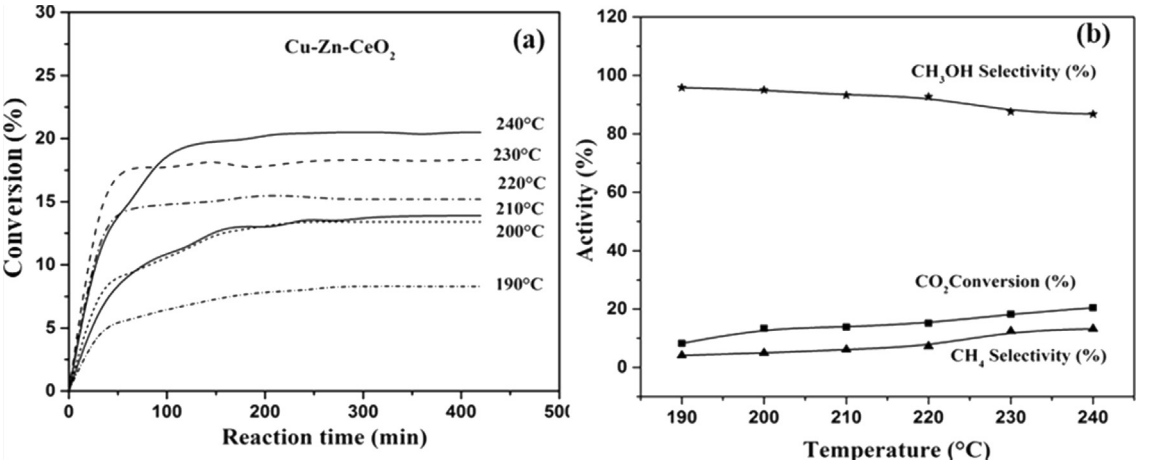

Fig. 10. a) CO_2 conversion as a function of the time and temperature of a reaction (b) MeOH and CH_4 selectivity as a function of the temperature of a reaction, over the $CuO-ZnO-CeO_2$ catalyst: flow = 1 L h^{-1} and $P = 1$ atm.

indicated that the stationary state is going to reach up (maximum CO_2 conversion). A slightly different behavior was observed for the test performed at 240 °C in which the approach to the maximum conversion was slower and characterized by a change in the slope. By increasing the temperature, the selectivity to CH_4 increased, whereas the methanol selectivity decreased simultaneously (Fig. 10b). Methanol selectivity was favored at low temperature; MeOH is indeed unstable at high temperature and is transformed into CH_4 and H_2O (in the presence of hydrogen) through the following successive reactions:

$$CO_2 + H_2 \rightarrow CH_3OH + H_2 \rightarrow CH_4 + H_2O$$

This transformation explains also the change in slope of the CO_2 conversion curve in Fig. 10a; at first the slope of the 240 °C curve followed that of the curves at lower temperature, whereas when the transformation to CH_4 started, the slope decreased and the rate for reaching the stationary state slowed down.

4. Conclusions

The catalysts prepared by the polyol method, and reported in the present research, presented improved properties in terms of metal oxide dispersion and morphology (i.e. sponge-like shape for the CeO_2-containing catalysts), and a variety of the metal and metal oxide species on the surface. Moreover, the CuO–ZnO–CeO_2 and Cu–ZnO–Al_2O_3 catalysts exhibited a higher activity and selectivity in the methanol synthesis by CO_2 hydrogenation than those displayed by catalysts prepared by more conventional methods, as summarized in Table 3. The results obtained for the catalysts prepared in the present work are also reported for comparison.

The most part of the catalysts listed in Table 3 presented CO_2 conversion <20% and selectivity to methanol <65%, even when the reaction was performed at a relatively high pressure (1.5–5.0 MPa), a more favorable condition than that used in the present research. It is worth to notice that on catalysts prepared by impregnation [42], the reaction performed at atmospheric pressure and with a H_2/CO_2 ratio of 9 allowed us to obtain only 12% conversion and 70% selectivity to methanol at 240 °C, confirming that polyol method is promising for the preparation of active catalysts for CO_2 hydrogenation (20% CO_2 conversion and 90% selectivity to MeOH).

Acknowledgments

All physicochemical characterizations were performed by the technical platforms of IS2M. The authors are very grateful to S. Hajjar, L. Josien, L. Michelin, and H. Nouali for their contribution.

References

[1] N. Yang, R. Wang, J. Clean. Prod. 103 (2015) 784–792.
[2] I. Melian-Cabrera, M.L. Granados, J.L.G. Fierro, J. Catal. 210 (2002) 285–294.
[3] M. Matzen, Y. Demirel, J. Clean. Prod. 139 (2016) 1068–1077.
[4] M.J. Bos, D.W.F. Brilman, Chem. Eng. J. 278 (2015) 527–532.
[5] W. Wang, S. Wang, X. Ma, J. Gong, Chem. Soc. Rev. 40 (2011) 3703–3727.
[6] T. Witoon, T. Permsirivanich, N. Kanjanasoontorn, C. Akkaraphataworn, A. Seubsai, K. Faungnawakij, C. Warakulwit, M. Chareonpanich, J. Limtrakul, Catal. Sci. Technol. 5 (2015) 2347–2357.
[7] G.A. Olah, A. Goeppert, G.S. Prakash, J. Org. Chem. 74 (2008) 487–498.
[8] K.C. Waugh, Catal. Lett. 142 (2012) 1153–1166.
[9] J.B. Hansen, P.E.H. Nielsen, in: G. Ertl, H. Knözinger, F. Schüth, J. Weitkamp (Eds.), Handbook of Heterogeneous Catalysis, Wiley-VCH Verlag GmbH & Co. KGaA, Weinheim, Germany, 2008.
[10] H. Arakawa, J.-L. Dubois, K. Sayama, Energy Convers. Manag. 1933 (1992) 521–528.
[11] M. Saito, T. Fujitani, I. Takahara, T. Watanabe, M. Takeuchi, Y. Kanai, K. Moriya, T. Kakumoto, Energy Convers. Manag. 36 (1995) 577–580.
[12] K.-W. Jun, W.-J. Shen, K.-W. Lee, T. Inui, H. Hara, T. Takeguchi, J.B. Kim, Korean Chem. Soc. 20 (1999) 993–998.
[13] K. Ushikoshi, K. Mori, T. Watanabe, M. Takeuchi, M. Saito, Stud. Surf. Sci. Catal. 114 (1998) 357–362.
[14] T. Witoon, T. Permsirivanich, W. Donphai, A. Jaree, M. Chareonpanich, Fuel Process. Technol. 116 (2013) 72–78.
[15] X. Dong, F. Li, N. Zhao, F. Xiao, J. Wang, Y. Tan, Appl. Catal. B 191 (2016) 8–17.
[16] L. Li, D. Mao, J. Yu, X. Guo, J. Power Sources 279 (2015) 394–404.
[17] X. Guo, D. Mao, G. Lu, S. Wang, G. Wu, Catal. Commun. 12 (2011) 1095–1098.
[18] A. Ateka, I. Sierra, J. Ereña, J. Bilbao, A.T. Aguayo, Fuel Process. Technol. 152 (2016) 34–45.
[19] V. Deerattrakul, P. Dittanet, M. Sawangphruk, P. Kongkachuichay, J. CO_2 Utilization 16 (2016) 104–113.
[20] L.X. Zhang, Y.C. Zhang, S.Y. Chen, J. Fuel Chem. Technol. 39 (2011) 912–917.
[21] C. Huang, S. Chen, X. Fei, D. Liu, Y. Zhang, J. Catal. 5 (2015) 1846–1861.
[22] B.J. Liaw, Y.Z. Chen, J. Appl. Catal. A. 206 (2001) 245–256.
[23] P.S.S. Prasad, J.W. Bae, K.W. Jun, K.W. Lee, J. Catal. Surv. Asia 12 (2008) 170–183.
[24] T. Inoue, T. Iizuka, K. Tanabe, Bull. Chem. Soc. Jpn. 60 (1987) 2663–2664.
[25] I. Melian-Cabrera, M. Lopez Granados, P. Terreros, J.L.G. Fierro, Catal. Today 45 (1998) 251–256.
[26] B. Denise, R.P.A. Sneeden, Appl. Catal. 28 (1985) 235–239.
[27] E. Ramaroson, R. Kieffer, A. Kiennemenn, Appl. Catal. 4 (1982) 281–286.
[28] F. Arena, K. Barbera, G. Italiano, G. Bonura, L. Spadaro, F. Frusteri, J. Catal. 249 (2007) 185–194.
[29] X.M. Liu, G.Q. Lu, Z.F. Yan, J. Beltramini, Ind. Eng. Chem. Res. 42 (2003) 6518–6530.
[30] Z.S. Hong, Y. Cao, J.F. Deng, K.N. Fan, Catal. Lett. 82 (2002) 37–44.
[31] C.L. Chiang, K.S. Lin, H.W. Chuang, J. Clean. Prod. 172 (2018) 1957–1977.
[32] Y. Nitta, T. Fujimatsu, Y. Okamoto, T. Imanaka, Catal. Lett. 17 (1993) 157–165.
[33] J. Słoczynski, R. Grabowski, A. Kozłowska, P. Olszewski, J. Stoch, J. Skrzypek, M. Lachowska, Appl. Catal. A 278 (2004) 11–23.
[34] J. Słoczynski, R. Grabowski, A. Kozłowska, P. Olszewski, M. Lachowska, J. Skrzypek, J. Stoch, Appl. Catal. A 249 (2003) 129–138.
[35] R. Raudaskoski, M.V. Niemelä, R.L. Keiski, Top. Catal. 45 (2007) 57–60.
[36] Y. Choi, K. Futagami, T. Fujitani, J. Nakamura, Appl. Catal. A 208 (2001) 163–167.
[37] G.X. Qi, J.H. Fei, X.M. Zheng, Z.Y. Hou, Chin. Chem. Lett. 12 (2001) 537–540.
[38] R.A. Köppel, C. Stöcker, A. Baiker, J. Catal. 179 (1998) 515–527.
[39] C.L. Carnes, K.J. Klabunde, J. Mol. Catal. A Chem. 194 (2003) 227–236.
[40] H. Lei, Z. Hou, J. Xie, Fuel 164 (2016) 191–198.
[41] L. Angelo, M. Girleanu, O. Ersen, C. Serra, K. Parkhomenko, A.C. Roger, Catal. Today 270 (2016) 59–67.
[42] J. Díez-Ramírez, F. Dorado, A.R. de la Osa, J.L. Valverde, P. Sánchez, Ind. Eng. Chem. Res. 56 (2017) 1979–1987.
[43] M. Lortie, R. Isaifan, Y. Liu, S. Mommers, Int. J. Chem. Eng. 2015 (2015) 750689, https://doi.org/10.1155/2015/750689, 9 pages.
[44] Y. Jeong, J.Y. Kang, I. Kim, H. Jeong, J.K. Park, J.H. Park, J.C. Jung, Korean J. Chem. Eng. 33 (2016) 114–119.
[45] H.S. Wu, S.C. Chung, J. Comb. Chem. 9 (2007) 990–997.

[46] B.K. Park, S. Jeong, D. Kim, J. Moon, S. Lim, J.S. Kim, J. Colloid Interface Sci. 311 (2007) 417–424.
[47] T.G. Altinçekiç, I. Boz, Bull. Mater. Sci. 31 (2008) 619–624.
[48] L.F. Bobadilla, C. Garcia, J.J. Delgado, O. Sanz, F. Romero-Sarria, M.A. Centeno, J.A. Odriozola, J. Magn. Magn. Mater. 324 (2012) 4011–4018.
[49] C.Y. Lu, H.H. Tseng, M.Y. Wey, L.Y. Liu, K.H. Chuang, Mater. Sci. Eng. B 157 (2009) 105–112.
[50] K.H. Chuang, K. Shih, C.Y. Lu, M.Y. Wey, Int. J. Hydrogen Energy 38 (2013) 100–108.
[51] K.C. Song, S.M. Lee, T.S. Park, B.S. Lee, Korean J. Chem. Eng. 26 (2009) 153–155.
[52] J.H. Byeon, Y.W. Kim, Ultrason. Sonochem. 19 (2012) 209–215.
[53] I. Boz, T.G. Altınçekiç, React. Kinet. Mech. Catal. 102 (2011) 195–205.
[54] E. Bayrakdar, T.G. Altınçekiç, M.A.F. Öksüzömer, Fuel Process. Technol. 110 (2013) 167–175.
[55] S. Brunauer, S.P.H. Emmett, E. Teller, J. Am. Chem. Soc. 60 (1938) 309–319.
[56] E.P. Barrett, L.G. Joyner, P.P. Halenda, J. Am. Chem. Soc. 73 (1951) 373–380.
[57] S.B. Bagherzadeh, M. Haghighi, N. Rahemi, Energy Convers. Manag. 134 (2017) 88–102.
[58] B. Ouyang, W. Tan, B. Liu, Catal. Commun. 95 (2017) 36–39.
[59] H. Ajamein, M. Haghighi, Energy Convers. Manag. 118 (2016) 231–242.
[60] J. Xiao, D. Mao, X. Guo, J. Yu, Appl. Surf. Sci. 338 (2015) 146–153.
[61] T. Witoon, N. Kachaban, W. Donphai, P. Kidkhunthod, K. Faungnawakij, M. Chareonpanich, J. Limtrakul, Energy Convers. Manag. 118 (2016) 21–31.
[62] J. Aguado, M.C. Castro, Microporous Mesoporous Mater. 128 (2010) 48–55.
[63] V. Deerattrakul, P. Dittanet, M. Sawangphruk, P. Kongkachuichay, J. CO_2 Util. 16 (2016) 104–113.
[64] F. Prinetto, G. Ghiotti, P. Graffin, D. Tichit, Microporous Mesoporous Mater. 39 (2000) 229–247.
[65] Y. Zhu, X. Kong, D.B. Cao, J. Cui, Y. Zhu, Y.W. Li, ACS Catal. 4 (2014) 3675–3681.
[66] J. Liu, C.H. Han, X. Yang, G. Gao, Q. Shi, M. Tong, C. Li, J. Catal. 33 (2016) 162–170.
[67] X. Dong, F. Li, N. Zhao, Y. Tan, J. Wang, F. Xiao, J. Catal. 38 (2017) 717–725.
[68] B. Zhang, Y.L. Zhu, G.Q. Ding, H.Y. Zheng, Y.W. Li, Appl. Catal. A 443 (2012) 191–201.
[69] S. Murcia-Mascarós, R.M. Navarro, L. Gomez-Sainero, J. Catal. 198 (2001) 338–347.
[70] K. Sun, K.W. Lu, F. Qiu, S. Liu, X. Xu, Appl. Catal. A. 252 (2003) 243–249.
[71] R.M. Friedman, J.J. Freeman, F.W. Lytle, J. Catal. 55 (1978) 10–28.
[72] M.C. Biesinger, L.W. Lau, A.R. Gerson, R.S.C. Smart, Appl. Surf. Sci. 257 (2010) 887–898.
[73] Y.K. Gao, F. Traeger, O. Shekhah, H. Idriss, C. Wöll, J. Colloid Interface Sci. 338 (2009) 16–21.
[74] C. Yang, F. Bebensee, J. Chen, X. Yu, A. Nefedov, C. Woll, Chem-PhysChem 18 (2017) 1874–1880.
[75] L. Óvári, S.K. Calderon, Y. Lykhach, J. Libuda, A. Erdőhelyi, C. Papp, H.P. Steinrück, J. Catal. 307 (2013) 132–139.
[76] A. Pfau, K.D. Schierbaum, Surf. Sci. 321 (1994) 71–81.
[77] P. Burroughs, A. Hamnett, A.F. Orchard, G. Thorton, J. Chem. Soc. Dalton Trans. 17 (1976) 1686–1698.
[78] C.J. Nelin, P.S. Bagus, E.S. Ilton, S.A. Chambers, H. Kuhlenbeck, H.J. Freund, Int. J. Quantum Chem. 110 (2010) 2752–2764.
[79] J.C. Frost, Nature 334 (1988) 577–580.
[80] R. Burch, R.J. Chappell, S.E. Golunski, J. Chem. Soc. Faraday Trans. 1 85 (1989) 3569–3578.
[81] R. Burch, R.J. Chappell, S.E. Golunski, Catal. Lett. 12 (1988) 439–443.
[82] X. Li, Z.J. Zhao, L. Zeng, J. Zhao, H. Tian, S. Chen, K. Li, S. Sang, J. Gong, Chem. Sci. 9 (2018) 3426–3437.
[83] H. Lei, R. Nie, G. Wu, Z. Hou, Fuel 154 (2015) 161–166.
[84] E.J. Choi, Y.H. Lee, D.W. Lee, D.J. Moon, K.Y. Lee, Mol. Catal. 434 (2017) 146–153.
[85] W. Wu, K. Xie, D. Sun, X. Li, F. Fang, Ind. Eng. Chem. Res. 56 (2017) 8216–8223.
[86] S. Soisuwan, W. Wisaijorn, C. Nimnul, O. Maunghimpan, P. Praserthdam, Eng. J. 20 (2016) 39–48.